




<https://doi.org/10.1038/s43247-024-01694-z>

A coupled atmosphere-ocean source mechanism was a predictor of the 2022 Tonga volcanic tsunami



Y. Tony Song  , Philip S. Callahan, Jean-Damien M. Desjonquieres, Severine Fournier & Josh K. Willis 

Volcanic tsunamis pose significant threats to nearby coastal communities. Despite extensive research, the mechanism behind tsunami generation remains unclear, and the ability to forecast a destructive tsunami has proven elusive. Here we present findings from the 2022 Tonga volcanic incident, showing that the leading air-pressure wave holds promise as a key predictor of tsunami behavior. We constructed an integrated atmosphere-ocean model to explain the underlying mechanism and validated it with various data, including satellite altimetry measurements. Contrary to prior hypotheses, our results reveal that: (1) the eruption process governs both the air-pressure and tsunami dynamics; and (2) the resulting crater volume controls the volcanic ejecta that produces the air-pressure waves, while the corresponding mass loss in the ocean triggers influxes of water into the crater, generating the tsunami. This study unveils a coupled atmosphere-ocean source mechanism in generating volcanic tsunamis and advocates for incorporating air-pressure sensors into early warning systems.

The Hunga-Tonga Hunga-Ha'apai (HTHH) volcano, situated at 20.546°S and 175.390°W, ~65 km northwest of Tongatapu, Tonga, commenced its eruption at 4:07 UTC on 15 January 2022¹ (Fig. 1a, b). NASA satellite imagery indicated intermittent eruption activity lasting for hours^{2–4}. Seismometers recorded eruptions, equivalent to a 5.8-magnitude earthquake (<https://earthquake.usgs.gov/earthquakes/eventpage/us7000gc8r/executive>). The eruptions generated global atmospheric Lamb waves, detected circulating the planet multiple times^{5,6}. Swift-traveling oceanic waves triggered tsunami alerts across the Pacific Ocean, resulting in minor impacts in distant areas^{7,8}. Near the volcano, however, the eruption was destructive. The near-field tsunami caused the deaths of three people and significant destruction to many low-lying coastal communities in Tongatapu, 'Eua, and the Ha'apai Group of Tonga. The tsunami runup height reached 15 m at Mango Island, and the inundation extended to 500 m inland, as reported by the Tonga Geological Services⁹. The volcanic eruption, tsunami, and ashfall caused an estimated US\$90.4 M in damages, the equivalent of ~18.5% of Tonga's Gross Domestic Product¹⁰.

The most widely known volcanic eruption is the 1883 Krakatau event, which generated a global-scale tsunami with a maximum wave height of 5.15 m at Jakarta, recorded by a tide gauge¹¹. The resulting devastation claimed over 36,000 lives, primarily through the subsequent tsunami, obliterating 300 villages around Indonesia's Sunda Strait between Java and Sumatra¹². The 1883 volcanic eruption also generated a large atmospheric wave or lamb wave with significant oscillations in pressure over nine days as

recorded by barometers in Europe and the United States^{13,14}. On 22 December 2018, the Anak Krakatau ("Child of Krakatau") erupted anew and triggered a smaller yet still deadly tsunami. This event caused 431 fatalities, and 7200 injuries, and displaced 46,646 individuals¹⁵. The eruption induced a Mw 5.1 earthquake in the regional seismic network¹⁶. Globally, nineteen events of volcanic tsunamis have been recorded since the instrumental era¹⁷.

Since the 1883 Krakatau incident, the formation of tsunamis via volcanic eruptions has remained a captivating enigma. Previous studies have suggested at least eight formation mechanisms^{17–20}. These include subaerial landslides, submarine landslides, pyroclastic flows, caldera or flank collapses, collapses of eruptive column, deep-ocean explosions, volcano-tectonic earthquakes, and the atmospheric origin of air-pressure waves. In the immediate aftermath of the 2022 Tonga volcanic incident, several of these mechanisms were employed to replicate the tsunami phenomenon. For instance, Omira et al.²¹ and Ren et al.²² demonstrated the atmospheric origin of the tsunami by simulating the Proudman resonance effect of air-pressure waves over deep-ocean trenches. Pakoksung et al.²³ and Purkis et al.²⁴ simulated the tsunami by the submarine explosion scenario without the atmospheric effect. Their simulations involved either a single explosion of 25 megatons or three increasingly larger explosions of 0.5, 4, and 15 megatons, respectively. In contrast, Lynett et al.²⁵ suggested multiple mechanisms for the tsunami by prescribing the air pressure and tsunami initial conditions separately.

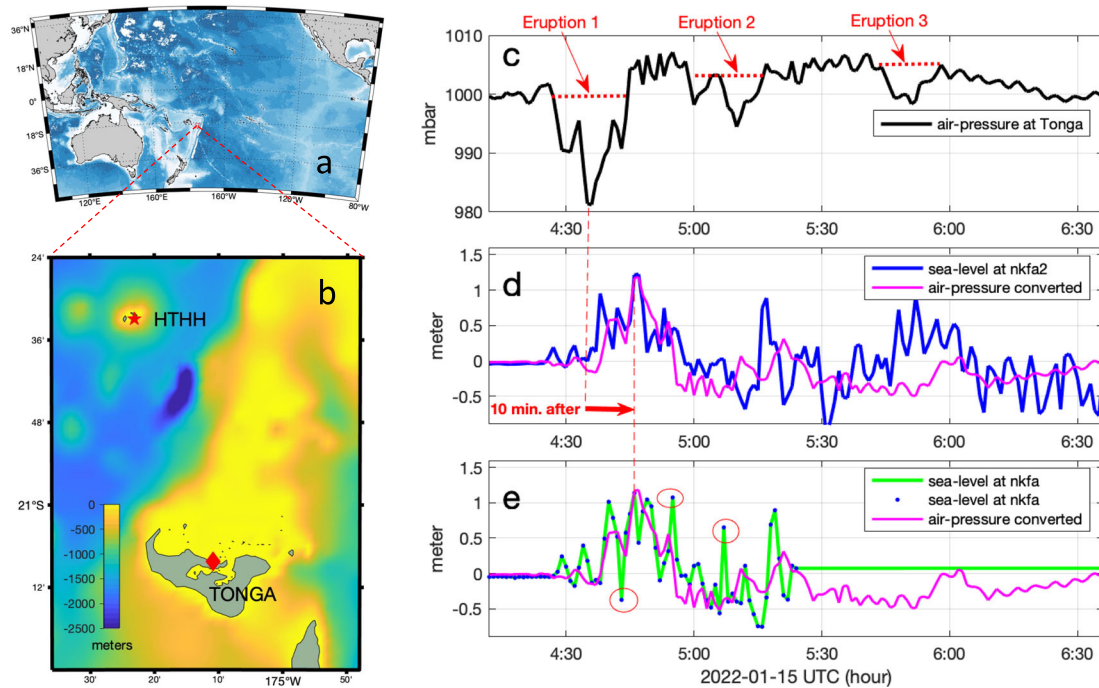


Fig. 1 | Air-pressure and tide-gauge in Tonga. **a** Location of the HTHH volcano. **b** Close-up of the local bathymetry, with the red diamond indicating the location of the Tonga tide-gauge. **c** Air-pressure data from Tonga, showing three distinct troughs corresponding to significant eruption cycles starting at 4:26, 5:01, and 5:46, each lasting approximately 20 minutes. **d** Tide-gauge data from Tonga (nkfa2

station) compared with air pressure-converted sea level (magenta, by Eqs. (1), (2)). **e** Tide-gauge data from Tonga (nkfa station) compared with air pressure-converted sea level (magenta, by Eqs. (1), (2)). Note that the nkfa tide gauge (green) malfunctioned at 5:25, with red circles indicating data points outside the expected range, likely due to the malfunction.

While the basic principle of tsunami generation necessitates the displacement of a substantial water volume, it's worth noting that before the eruption, the HTHH volcano was positioned partially above sea level with minimal water above the crater (Supplementary Fig. S1). This geophysical setting contradicts the typical scenario of deep-ocean explosions triggering tsunamis. Adding to the enigma, recent seafloor surveys of the volcano have shown no substantial indications of caldera or flank collapses^{26,27}. The survey team discovered that the volcano's rim was remarkably intact, with no signs of significant deep-ocean explosions²⁸. On the other hand, the effects of air-pressure waves on sea levels have been well understood and characterized by moving origins with Lamb waves²⁹, but these have been observed globally with small amplitudes of a few centimeters, which cannot explain the near-field destruction of the volcanic tsunami³⁰.

The central question is how the volcanic eruption managed to trigger such a destructive tsunami with a relatively small amount of water present. Despite the discovery of the Lamb wave over a century ago in 1881¹³, its connection to volcanic tsunamis at the source region remains elusive. These uncertainties surrounding the genesis of tsunamis and air-pressure waves underscore the challenges in predicting volcanic tsunamis effectively to safeguard lives. Understanding the source mechanism of generating Lamb waves and volcanic tsunamis has been challenging due to the logistical difficulties of collecting near-field data during eruptions. Without fully understanding the forming mechanism, developing a predictive approach for early warning is difficult.

In this study, we found an intrinsic coupling between air-pressure waves and tsunamis at the source region during their formation. Using an integrated atmosphere-ocean model, we show that this coupling originates from the volcanic ejection process, which causes lateral explosions of air to form air-pressure waves and a proportional influx of water in the ocean to trigger tsunamis. Since the volcanic ejecta results from the mass loss in the ocean, the principle of mass conservation allows fast-moving air-pressure waves to provide predictive insights for tsunamis. This coupled atmosphere-ocean source mechanism is distinct from previously proposed mechanisms, offering a novel understanding of volcanic

tsunami genesis and the potential for early warning systems in the near field, where most fatalities occur.

Results

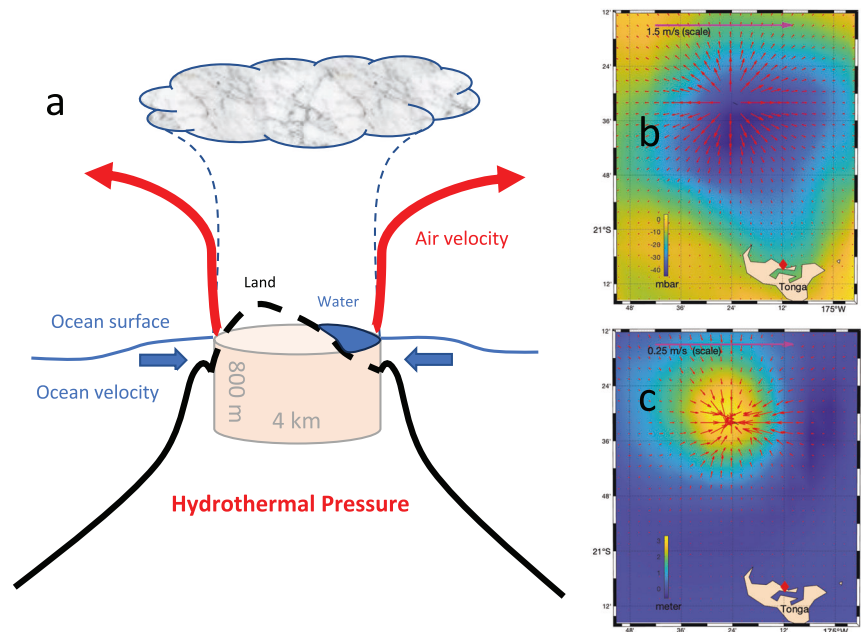
Air-pressure and tsunami connection

We found that the air-pressure waves (Fig. 1c), measured from the Tonga meteorological station, after converted into sea-level (by Eqs. (1), (2)), predict the Tonga tide-gauge-recorded tsunamis well in both strength and waveforms (Fig. 1d, e). The air-pressure data originates from the Tonga Meteorological Office, while the tide-gauge measurements at NuKu'alofa waterfront (nkfa) and Vuna Wharf (nkfa2) stations were sourced from <https://www.ioc-sealevelmonitoring.org/> (Supplementary Figs. S2 and S3). Notably, the three instances of low air pressure correspond closely to the respective heights of the tsunami recorded by the tide gauges. The three pressure lows indicate three major eruptions at HTHH. The correlation exhibits exceptional accuracy in the first wave (Supplementary Fig. S4), but less so in subsequent waves due to the resonance effects of the first and largest wave within the vicinity of Tonga's islands and harbors. When it comes to tsunami warnings, the primary concern is the largest wave. The nkfa tide gauge experienced malfunctioning at 5:25 UTC, but still captured the first and the second waves, which confirms the correlation between the air-pressure wave and the tsunami.

The prediction is formulated as follows. First, we converted the air pressure (black line in Fig. 1c) into sea-level anomaly (magenta in Fig. 1d, e) based on the principle of inverted barometer (IB) effect, i.e., an increase in air pressure (p_a) of 1 mbar (or hPa) corresponds to a surface depression of approximately 1 cm. Mathematically, the effect of the air pressure on the sea level can be written as $\eta^{ib} = -p_a/g\rho$, where ρ is the water density, and g is the gravity coefficient. This formula converts the atmospheric pressure anomaly into the thickness of water. We then convert the thickness of water into a tsunami with the empirical tsunami runup formula at the Tonga coast³¹:

$$\eta(t + \tau) = -(p_a(t)/g\rho)R_f \quad (1)$$

Fig. 2 | Formation of air-pressure wave and oceanic tsunami. **a** Schematic of the coupled atmosphere-ocean source mechanism during the volcanic eruption. The brown cylinder, 4 km in diameter and 800 m deep, presents the crater formed by the volcanic ejection of water, gases, and magma into the atmosphere. The red arrows indicate the mass gained by the atmosphere and the resulting air expansion that triggers air-pressure waves. The blue arrows show water velocity as it fills the oceanic cavity, generating the tsunami. **b** Depth-averaged air velocity, depicted by red arrows, illustrates the lateral blast as air radiates away from the crater. The background color corresponds to the air pressure anomaly (lower pressure) one minute after initialization. **c** Depth-averaged water velocity, represented by red arrows, shows the influx of ocean water toward the crater. The background color reflects the sea level anomaly (higher sea level) one minute after initialization.



Here R_f is the empirical runup factor, t is the time, and $\tau = d/v_o - d/v_a$ is the lead time of the air-pressure wave over the tsunami at the measurement location, in which d is the distance from the volcano, v_a and v_o are the travel speed of the air-pressure wave and the tsunami, respectively. We have used the calibrated formulation based on coastal measurements³²:

$$R_f = 1.29 \left(\tan(\alpha) \sqrt{L_o/H_o} \right)^{0.72} \quad (2)$$

Here L_o is the wavelength, H_o is the significant tsunami height, and α is the slope angle. Their values are 40 km, 1.2 m, and 3.6 degrees in the Tonga case, like those used in previous studies^{31,32}.

Note that air-pressure waves travel in the atmosphere with negligible effect on the coast and land. Differently, tsunamis become slower and increase in height toward the coast. Both air pressure and tsunami travel speed can be estimated precisely as the atmosphere and ocean depth are known³³. Tonga is located ~65 km from the volcano. The speed of the air-pressure wave is ~330 m/s, traveling in the atmosphere with an averaged depth of 11.2 km. The speed of the tsunami is about 82 m/s in the near field, based on bathymetry data that has an average depth of 680 m from the volcano to Tonga. The arrival time was 3 minutes for the air-pressure wave and 13 minutes for the tsunami, respectively. The air-pressure lead time is about 10 minutes, which is used in Eqs. (1), (2), aligning well with the actual data observed in Tonga.

Coupled atmosphere-ocean source mechanism

To explain the physical connections between the air-pressure wave and the tsunami, we constructed an integrated atmosphere-ocean model based on the open-source code of the Regional Ocean Modeling System (ROMS), which is available online (www.myroms.org). ROMS is a full hydrodynamic ocean general circulation model, mainly used in the oceanography community for various applications^{34,35}. For tsunami simulation, the shallow-water equation module with a constant water density is used, which is like the widely used tsunami model of Satake³⁶. In this study, we used 12-vertical levels for the water column—a similar setting used in previous studies of the 2004 Indian Ocean tsunami and the 2011 Japan tsunami^{37,38}.

For the atmospheric pressure waves (or Lamb waves), we used the same ROMS model, but replaced the ocean depth (bathymetry) with the atmosphere depth. Following Amores et al.³⁹, the

atmosphere depth can be derived by

$$H_A = \frac{\gamma \cdot R \cdot T}{M \cdot g}, \quad (3)$$

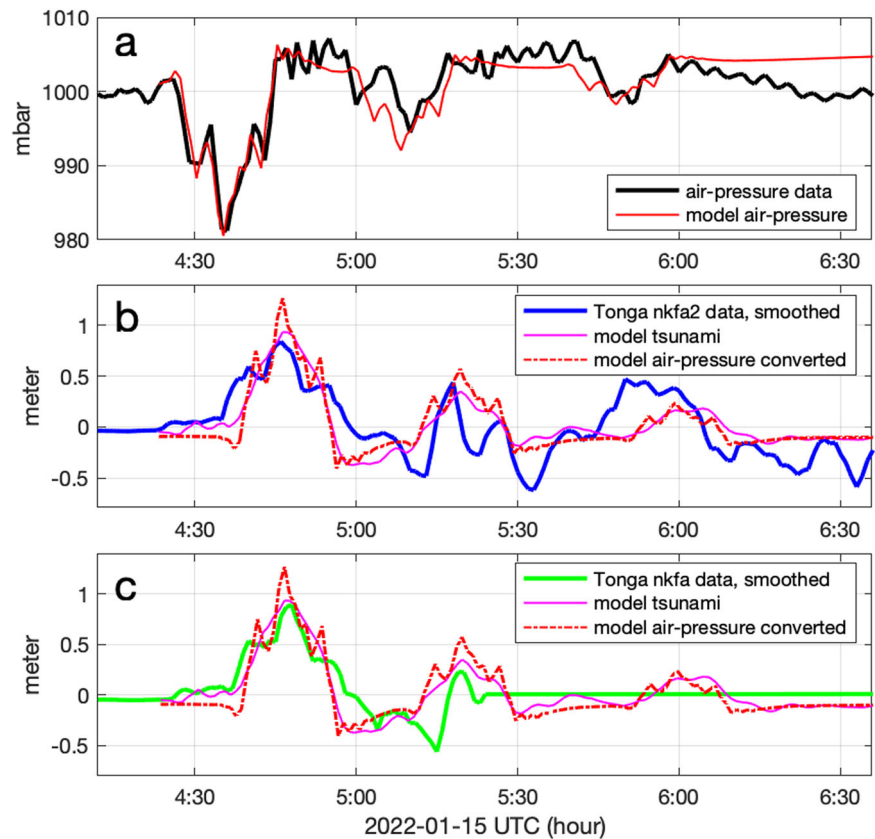
where $\gamma = 1.4$ is the nondimensional ratio of specific heat of air corresponding to the range of atmospheric temperatures, $R = 8314.36$ J/kmol/K is the universal gas constant, T is the absolute temperature, with a mean value of 273.15, and $M = 28.966$ kg/kmol is the molecular mass for dry air. The mean atmosphere depth is ~11189.24 m. The atmosphere pressure is converted into equivalent water thickness by a factor of $1/g\rho$, meaning 1 millibar corresponds to 1 centimeter of water thickness.

We initialized the atmosphere and ocean model by the same sequence of eruption process, but with an opposite orientation of initial velocity field (Method 1), as schematically shown in Fig. 2a. Note that both the atmosphere and ocean models are the depth-averaged shallow-water-equation model. Their progressive variables are the surface elevation η and the depth-averaged velocity (U , V), representing the air-pressure wave and depth-averaged air velocity in the atmosphere, as well as the sea-level (or tsunami) and depth-averaged ocean velocity in the ocean, respectively. The air-pressure wave and the tsunami can be initialized either by a perturbation of the surface η or the velocity (U , V)³⁷. In our case, the atmosphere model is initialized by a depth-averaged air velocity away from the crater, while the tsunami model is initialized by a depth-averaged ocean velocity toward the crater, respectively (Fig. 2b, c).

In the atmosphere model, the outward initial velocity field represents lateral explosions of air extending far beyond the volcanic rim. This is consistent with satellite images, which show the radiative aerosols expanded hundreds of kilometers in the sky^{2–5}. The initial conditions represent three sequences of volcanic eruptions for a period of 20 minutes, with strength reduced by a half in each period, as suggested by the Tonga air-pressure data. Air pressure caused by volcano eruption is primarily a low-pressure system at Earth's surface—the atmospheric base. The atmospheric model generates a negative air-pressure anomaly, as shown by the background color with a minimum of 35 mbar (Fig. 2b). This air-pressure IB is applied to ocean model as the sea-surface condition.

In the ocean model, the initial velocity field is an influx field toward the crater, opposite to the initial atmosphere field, representing the movement of the ocean water to fill up the erupted cavity (Fig. 2c).

Fig. 3 | Comparison of modeled air pressure and tsunami with Tonga data. a Comparison of air pressure. **b** Comparison of sea level at the nkfa2 station. **c** Comparison of sea level at the nkfa station. The dashed lines represent the air pressure-predicted tsunami based on Eqs. (1), (2).



The atmospheric and oceanic initial conditions are implemented at the same time sequence and resulted in an accumulated kinetic energy of 7.8×10^{15} Joule for the atmosphere and 3.5×10^{14} Joule for the ocean, respectively (Method 1).

We run the two models in parallel, and sum their results as the total (atmospheric and oceanic) tsunami,

$$\eta^{A+O} = -\eta^A + \eta^O$$

Here, η is the total sea-level anomaly or tsunami, where A and O indicate the components of atmospheric and oceanic tsunami, respectively. The negative sign of the atmospheric component represents the inverse barometer (IB) effect, resulting in a sea-level depression when there is a positive air-pressure anomaly. Removing the negative sign, $\eta^A + \eta^O$ represents the total ocean bottom pressure, where η^A is the equivalent air-pressure measurements on land adjusted by $g\rho$.

Figure 3 shows the simulated air-pressure wave and tsunami at the Tonga location, compared with the smoothed Tonga air-pressure and tide-gauge data to focus on the large features represented by the model. The model reproduced the data well in both strength and waveforms, suggesting that the correlation (Fig. S4) between the air-pressure wave and the tsunami have fundamental physical connections, at least in the near-field.

The model results were further validated by far-field observations, including the Deep-ocean Assessment and Reporting of Tsunamis (DART) data, air-pressure measurements on land, and satellite altimetry data. The DART system measures the ocean bottom pressure⁴⁰, which has been converted to the equivalent of water thickness in meters (i.e., $\eta^A + \eta^O$). We compared our model results with the DART measurements, showing that the integrated atmosphere-ocean model represents the magnitude and speed of the tsunami well (Fig. S5). These model-data comparisons confirm two specific types of tsunamis: the atmospheric tsunami, originating from the air-pressure effect, travels at the Lamb wave speed of 330 m/s. The oceanic tsunami, originating from volcanic eruptions, propagates at various

speeds depending on water depth, averaging 160 m/s. On land, air-pressure sensor data were accessible. Further comparisons of model air pressures (i.e., η^A) with extended data from surrounding islands of HTHH reveal consistent air pressure patterns and amplitudes (Fig. S6).

Because of the IB effect, sea-surface measurements of the atmospheric tsunami show the opposite anomaly compared to the DART measurements at the ocean bottom (i.e., $-\eta^A + \eta^O$, Method 2). Therefore, surface observations are crucial evidence for elucidating the mysterious role of air-pressure waves on tsunamis at sea level. Previously, satellite altimetry has demonstrated its capability to measure earthquake tsunamis⁴¹. Unlike in-situ measurements of DART and air-pressure gauges, satellite altimeters offer a synoptic view of the tsunami in the open ocean, often closer to the epicenter. The HTHH event was the first significant volcanic eruption to have occurred in the satellite era. We examined all possible satellite altimetry measurements that might have captured the surface displacement of the tsunamis, including the India-French satellite AltiKa, and the Jason-3 and Sentinel-6 Michael Freilich (S6A) satellite. We processed the data to compare with the model by co-locating the satellite passes with the model in time and location (Fig. 4 and Method 2). For the first time, we found that the satellite altimetry captured the tsunami on both near-field and far-field locations. The AltiKa satellite observed the tsunami within locations between 19°S and 28°S during 29–38 minutes after the eruption, while the S6A and Jason-3 satellites, 30 seconds apart, measured the tsunami through the volcano center, 5 hours after the eruption (Supplementary Fig. S7). Surprisingly, the tsunamis fell well within the range of typical ocean dynamic signals, suggesting that the destructive force of the volcanic tsunami might have diminished in these regions.

Discussion and conclusion

Genesis of air-pressure waves and oceanic tsunami

The primary evidence from the Tonga volcanic observations centers on the connection between the air-pressure wave and the tsunami, a connection at the source region previously unexplored. Our atmosphere-ocean model put

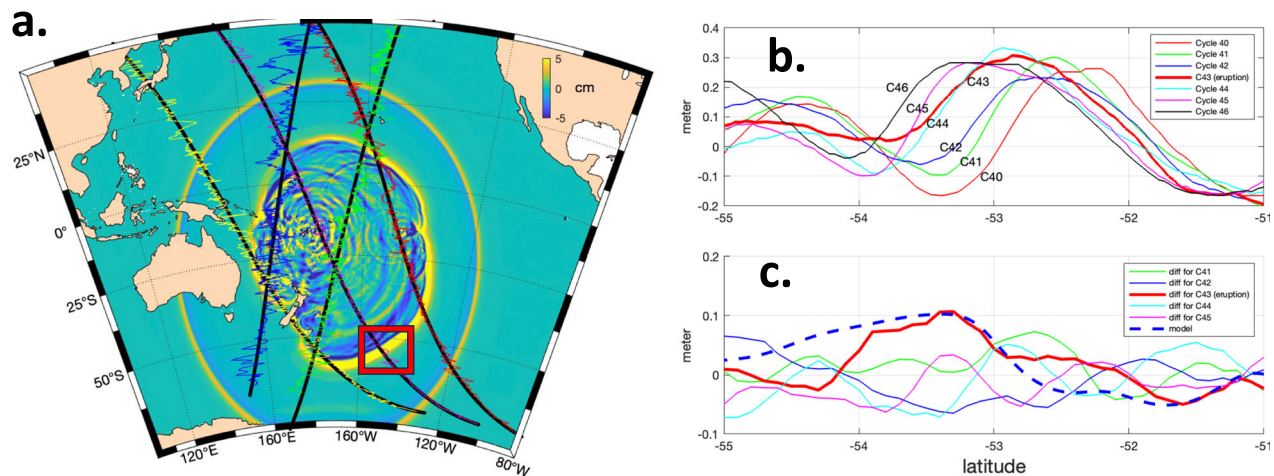


Fig. 4 | Satellite altimetry. **a** Satellite altimetry track overlaid on the model tsunami map for the day of the volcanic eruption. **b** Sea-surface height anomaly recorded by the S6A satellite within the highlighted red square on the map. Labels C40–C43 correspond to the satellite pass cycles. **c** Sea-surface height differences are calculated

by subtracting the pre- and post-eruption past cycles. The heavy red line represents the cycle on the day of the eruption, while the dashed line shows the modeled tsunami.

forth a novel explanation of the connection through a coupled atmosphere-ocean source mechanism during their formation process. In the atmosphere model, we employ the lateral blast mechanism—caused by the rapid expansion of air—to initiate the air pressure waves. This mechanism explains the satellite imagery showing the mushroom cloud in the sky during the eruptions. It is also corroborated by the wind data from the Tonga Met Office (Supplementary Fig. S2 (right)). The wind gust arrived in Tonga ~45 minutes after the eruption with a maximum speed of 40 m/s, suggesting the lateral movement of air by the eruption. Together, these lines of evidence consistently suggest a lateral forcing mechanism of hot air, resulting in the formation of a low-pressure center in the near-field and resulting in a high-pressure anomaly of lamb wave extending to the far fields (Supplementary Figs. S5 and 6)—a phenomenon unique to volcanic eruptions. This explanation sheds light on the mystery surrounding the generation of a lamb wave within an 11 km-depth atmosphere by a 4 km-sized volcano.

In the ocean, the situation becomes more intricate due to the formation of a water cavity during volcanic eruptions, ultimately resulting in an underwater crater. By the continuity principle of fluid flow, surrounding ocean waters must fill the water cavity, which would induce ocean mass movement necessary for the generation of the tsunami. Simultaneously, the large-scale low-pressure center above would raise the sea level upward. This causes lateral water movement towards the crater, further enhancing the mechanism to trigger the oceanic tsunami. Eyewitness reports of sea-level recession preceding the tsunami along the Tonga coast⁴² further corroborate this intricate atmosphere-ocean interplay, highlighting the initial movement of water towards the crater. This explanation sheds light on the puzzle of how volcanic eruptions, often occurring atop seamounts or partially above sea level, can trigger tsunamis despite the limited water volume present. Unlike earthquake-triggered tsunamis, which involve large-scale movement at the deep-ocean floor and exhibit transoceanic devastation potential³⁷, volcanic tsunamis possess a distinct characteristic: they are exceptionally destructive in the near field but comparatively less damaging in the far-field, despite their extensive reach due to the complexities of the Lamb wave effect during propagation. This distinction may be attributed to the coupled source mechanism and the surface forcing mechanism of atmosphere-ocean interplay, which resulting in a combined behavior akin to storm surges and earthquake-triggered tsunamis.

Pressure sensors for early warning

The intrinsic and measurable correlation between air pressure waves and volcanic tsunamis presents a promising avenue for predicting volcanic tsunamis using air pressure sensors. Specifically, our research demonstrates that

the mass ejected into the atmosphere during a volcanic eruption equals the mass lost in the ocean, establishing the basis for a quantitative and temporal link between air-pressure waves and tsunamis. This relationship is governed by the intensity of the eruption and the resulting crater size, while the air pressure wave is the front runner. In Fig. 5, we demonstrate the predictive skills of the air-pressure waves on near-field tsunamis using Eqs. (1), (2) and further validate these predictions with Fiji observations, where co-located air-pressure and sea-level measurements were available. We found that the air-pressure waves can predict tsunamis with lead times of 5 minutes, 10 minutes, and 50 minutes at distances of 30 km, 65 km (Tonga), and 280 km (Fiji–Suva) from HTHH, respectively. Particularly, the tide-gauge record at Suva shows three prominent peaks, marked by black arrows in Fig. 5d, which are consistent with the Tonga tide-gauge measurements, further validating the coupled atmosphere-ocean source mechanism.

Based on the Tonga data and post-event surveys^{9,26}, a volcanic air-pressure anomaly exceeding 15 mbar could indicate an impending destructive tsunami, as marked by the magenta dotted lines in Fig. 5b, c. This suggests that air-pressure sensors could be employed for volcanic tsunami early warning. For example, both the first and the second eruptions could generate destructive tsunamis within a 30 km range, necessitating the triggering of alarms for both eruption events in the closer location, while only the first event would require alarms in Tonga. Notably, the magnitudes of the air pressure wave and subsequent tsunamis at the closer location nearly double those observed in Tonga. This might explain the catastrophic outcomes in the incidents of 1883 and 2018, as many coastal settlements along the Indonesian Sunda region were situated within a 30-kilometer radius of the Krakatau volcanoes, much closer than Tonga is to HTHH. Had air-pressure sensors been integrated into the warning system, residents could have been alerted in each of these eruption events to save lives. Conversely, in Fiji, where the air pressure remained well within the alarm threshold, no warning was necessary, thus avoiding panic among residents. Reducing false alarms can have significant societal benefits by avoiding economic losses and increasing trust in the warning system.

Given the observational evidence and model demonstrations from the 2022 Tonga volcanic incident, it is strongly recommended to deploy air pressure sensors across coastal communities surrounding approximately ninety potentially tsunamigenic volcanoes worldwide¹⁷. Air-pressure sensors are inexpensive to install and have traditionally been maintained by weather forecasting agencies, which are also responsible for tsunami early warning. These sensors could serve to monitor volcanic activity, validate future research findings, and establish a baseline threshold for calibration. Should a volcanic eruption generate an air pressure anomaly surpassing the

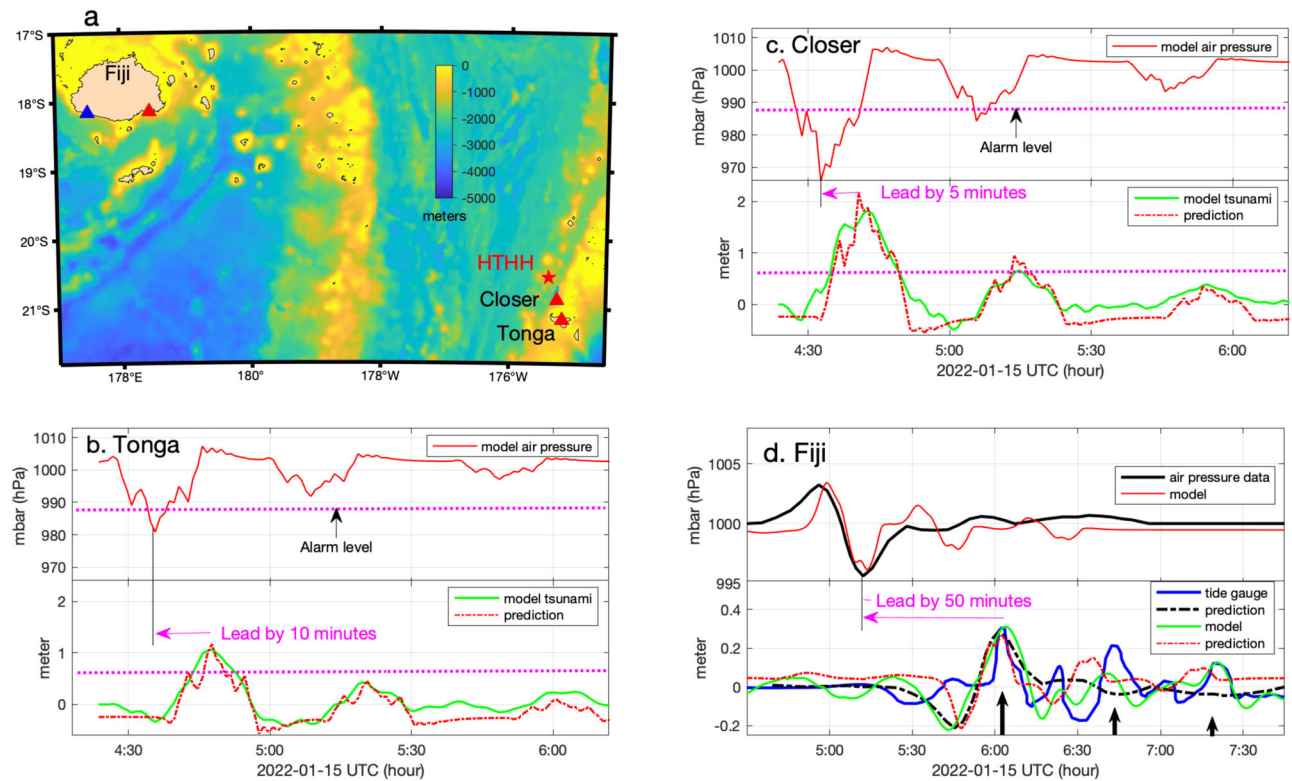


Fig. 5 | Air-pressure waves as predictors of tsunamis. **a** Co-located air-pressure sensors and tide-gauges (red triangles) around HTHH. **b** In Tonga, the air-pressure waves lead the tsunami by 10 minutes. **c** At a closer location, 30 km from HTHH, air-pressure waves lead the tsunami by 5 minutes. **d** In Suva, Fiji, air-pressure waves lead

the tsunami by 50 minutes (both data and model). The dashed lines represent tsunami predictions based on Eqs. (1), (2), with the dark lines representing data and the red lines representing the model results.

designated threshold, such as 15 mbar, an alert or alarm system could be activated to promptly notify and safeguard coastal residents. Indeed, throughout history, the devastating impacts of volcanic tsunamis have been predominantly confined to the near field of the eruption epicenter¹⁷. Satellite altimetry measurements have substantiated the confinement of the Tonga tsunami. Within the near-field perimeter, a lead time of ~5–10 minutes exists, providing a crucial window for evacuation measures.

Thanks to the unprecedented observational evidence from the recent Tonga incident, our study offers two innovative contributions: (A) The coupled atmosphere-ocean source mechanism provides a unified explanation for the simultaneous formation of air-pressure waves and volcanic tsunamis, enabling a re-examination of previous assumptions about historical events. (B) The predictive potential of the leading air-pressure waves for destructive tsunamis holds practical value. Our predictive formula, based on simple Eqs. (1), (2) and inexpensive air-pressure sensors, represents the first step toward a practical early warning system for volcanic tsunamis.

Methods

Method 1. Computing air-pressure and tsunami initial conditions

An integrated atmosphere-ocean model based on hydrodynamic equations (www.myroms.org) has been employed to demonstrate the coupled atmosphere-ocean source mechanism for generating air-pressure waves and associated volcanic tsunamis. The key lies in formulating the initial conditions for the atmosphere and ocean components of the model. Our method is detailed as follows.

We first used seismic data from the USGS website (<https://www.usgs.gov/natural-hazards/earthquake-hazards/earthquakes>) to determine the precise location of the volcanic eruption and the resulting seafloor deformation. The results are reproducible since seismic data are openly accessible to both the public and tsunami warning systems. Our seismic inversion technique follows the methodology outlined by Chen et al.^{43,44}, yielding a

magnitude of Mw 5.8 earthquake and a three-dimensional representation of seafloor deformations in the region (Supplementary Fig. S8). Notably, the inverted seafloor displacements are minimal, only a few centimeters around the crater, with uplift reaching ~10 centimeters. This minimal seafloor deformation rules out the possibility of the destructive Tonga tsunami being caused solely by earthquake forces. Nevertheless, the inversion solution serves to pinpoint the volcanic eruption's location and accounts for tectonic earthquake effects, if significant.

Subsequently, we utilized the seismic-inverted velocity field (U_s , V_s) of seafloor displacement to establish the initial conditions for the atmosphere and ocean model, respectively. In the case of a volcanic eruption, the initial disruption in both the atmosphere and ocean is the horizontal displacement of air and water. Initializing the two models with velocity fields is more appropriate than directly prescribing pressure and sea-level perturbations. Specifically, we projected the velocity field onto the model grid, and formulated the eruption process by a sinusoidal function, as detailed as follows.

For atmosphere, the initial condition is:

$$(U_A, V_A)(t) = \begin{cases} (U_s, V_s) \sin\left(\frac{\pi t}{T}\right) E_A, & t \leq T \\ 0, & \text{other} \end{cases} \quad (4)$$

For ocean, the initial condition is:

$$(U_O, V_O)(t) = \begin{cases} -(U_s, V_s) \sin\left(\frac{\pi t}{T}\right) E_O, & t \leq T \\ 0, & \text{other} \end{cases} \quad (5)$$

In above equations, (U_A, V_A) and (U_O, V_O) represent the depth-averaged air velocity and ocean water velocity, respectively. The variable t denotes time, and T represents the period of an eruption cycle. The positive

sign signifies the expulsion of air from the crater, while the negative sign indicates the influx of ocean water towards the crater to fill the cavity created by the eruption.

Analysis of Tonga air-pressure data and satellite imagery reveals three significant eruptions commencing at 4:26, 5:01, and 5:46. Each eruption lasts approximately 20 minutes, with intensity halving over time. Based on this data, we assume a duration of 20 minutes for each eruption cycle; hence, $T = 1200$ s. To represent these observations, we applied the initial conditions to the atmosphere and ocean model at each of the eruption commencing times, while reducing the intensity coefficients E_A and E_O by a half each cycle. The initial values of E_A and E_O are determined by fitting the model to the air-pressure data and tsunami measurements, resulting in a value of 0.05 and 0.17, respectively. The head and shoulder pattern of the air pressure (Fig. 1c–e) was reproduced by adding 50% of the E_A and E_O values at the corresponding time step during the initial period of the model.

The coupled initial conditions of Eqs. (4), (5) establish a quantitative relationship between the air-pressure waves and the tsunami within the integrated atmosphere-ocean model. This enables validation through the correlation of air-pressure measurements and tsunami data. Our model domain covers the entire Pacific Ocean, with an average grid size of 3 km, utilizing ETOPO2 for ocean bathymetry.

The resultant energy source (i.e., initially applied to the atmosphere and ocean system) can be calculated in the kinetic energy (KE) form:

$$KE = \frac{1}{2} \rho h \iint (U^2 + V^2) dx dy \quad (6)$$

where ρ and h are the density and depth of atmosphere and ocean, respectively. The spatial integral is for the source region, in which $dx dy$ is the grid size. The total energy can be obtained by integrating Eq. (6) over the eruption period, which has three eruption cycles in the Tonga case. Our calculation yields that the total atmospheric source energy is about 7.8×10^{15} Joule, while the ocean is about 3.5×10^{14} Joule.

The tsunami source energy also can be estimated by the crater volume. For instance, observational data shows that the crater has a diameter of 4 km and a depth of 800 m. This results in a volume of $\pi r^2 D \approx 10 \text{ km}^3$, where $r = 2$ km and $D = 0.8$ km. This volume of water must be displaced from around the volcano to the crater by influxes of water, represented by the flow field (U_O, V_O) in Eq. (5). This influx would cause a mass loss of water from a larger circular area $A = \pi R^2$, resulting in a sea-level depression of η around the volcano. The resultant potential energy (PE) is:

$$PE = \frac{1}{2} \rho g \eta^2 A. \quad (7)$$

For simplicity, we assume the sea-level depression is constant, thus ηA equals the crater volume. Given the convertibility of energy, we can assume PE equals KE, resulting in $\eta = 7$ meters and $R = 21.1$ km. A similar approach can be applied to calculate the atmospheric source energy.

Method 2. Satellite altimetry

Since the early 1990s, satellite radar altimeters have been providing measurements of sea-level anomaly with accuracy of ~ 1 cm after appropriate corrections⁴⁵. Such an accuracy easily detected the surface displacements (~ 150 cm) of the 2004 Indian Ocean tsunami and the 2011 Japanese tsunami^{38,41} but had not observed a volcanic tsunami yet. For volcanic tsunami, the sea-surface measurements are different from the ocean bottom pressure,

$$P_b = P_a + \int_{-h}^{\eta} \rho g dz \approx P_a + \eta \rho g + \int_{-h}^0 \rho g dz \quad (8)$$

where P_b is the total pressure at ocean bottom and P_a is the air pressure at sea surface, while η is the sea-level anomaly being measured by satellite

altimeters. At the mean sea level, Eq. (8) gives the IB formulation of $\eta^{ib} = -p_a/g\rho$, where p_a is the air-pressure anomaly. As the air-pressure wave (or lamb wave) could not be ignored in the volcanic tsunami, the altimetry measurements should be in the form of $\eta^{A+O} = -\eta^A + \eta^O$, where $\eta^A = p_a/g\rho$ and η^O are the atmospheric and oceanic tsunami, respectively.

For the Tonga volcanic tsunami, we have examined all possible satellite altimetry measurements that might have detected the surface displacement of the tsunamis and identified several passes which had the opportunity to capture the tsunamis (Fig. 4a). We processed the data to compare with the model by co-locating the satellite passes with the model in time and location. The SARAL/ALtiKa (Satellite with ARGOS and ALtiKa), a joint mission between the Indian Space Agency and the French Space Agency (CNES) launched on February 25, 2013, belongs to the global altimetry system for the precise and accurate observations of ocean circulation and sea-surface elevation (https://altika-saral.cnes.fr/en/SARAL/GP_mission.htm). Jason-3 and Sentinel-6 Michael Freilich (S6A) are joint missions between NASA, NOAA, EUMETSAT, ESA and CNES. They were launched on 17 January 2016, and 21 November 2020, respectively, with the objective of providing high-precision measurements of global sea-level for climate studies (<https://sealevel.jpl.nasa.gov>).

We found that the AltiKa satellite captured the near-field tsunami, ~ 38 minutes after the eruption, while the S6A and Jason-3 satellites in 30 seconds apart crossed the tsunami through the post-erupted volcano center, 5 hours after the eruption. We used tsunami travel times to isolate the tsunami signals from ocean dynamic features because altimetry data has both tsunami and ocean dynamic features, while the model only has the tsunami result.

We have used a cycle-differentiating method by comparing before and after-cycles of the altimetry passes, as shown in Fig. 4b for the S6A data as an example. In the ocean between 50°S and 60°S large ocean eddies are generated and interact with the fronts of the Antarctic Circumpolar Current, making detection of the tsunami signal difficult. The repeat cycle for these missions is 10 days between successive identical orbits. Because the eddies and fronts in the ocean move slowly over a period of 10–20 days⁴⁵, while tsunamis travel much faster. This speed difference helps identifying the tsunami fronts. Figure 4c shows the difference around the location of 53°S, where the tsunami propagates according to the travel time, cycle 43 has an abnormal shift in comparison with all prior and subsequent cycles. The difference between cycle 43 and cycle 42 stands out and is consistent with the location and amplitude of the modeled tsunami, confirming detection of the tsunami. Similar results have been obtained for the Jason-3 data, which is not shown here.

Note that AltiKa operated on a drifting cycle and did not follow the same orbit every 10 days; therefore, the cycle-differentiating is ineffective. As a result, the procedure for removing ocean dynamic signals within a 10-day window was not applied to the AltiKa data. This is why significant ocean dynamic signals within a 10-day period remained, as shown in Fig. S7a, b. Even without the differencing technique, the AltiKa sea surface shows good agreement with the model data. With the cycle-differentiating, we have processed the S6A and Jason-3 data. The S6A and Jason-3 were on the same pass, but in 30 seconds apart. Fig. S8c, d shows the pass 186 (descending), which was determined over the volcano after 5 hours of the eruption and then observed the tsunami front in the Southern Ocean at latitude of 53°S. Comparing the two satellites data with model (Supplementary Fig. S7e) shows the agreement of two prominent features: One at the volcano location ($\sim 20^\circ$ S) and the other at the estimated tsunami travel time in the Southern Ocean ($\sim 53^\circ$ S). The high waves at the volcano area suggest the resonance waves were still active after 5 hours of the eruption, while the tsunami front in the Southern Ocean indicates the strength of the tsunami propagating to the southeast direction.

Code availability

All figures were created with the Matlab software (<https://www.mathworks.com/products/matlab.html>), a licensed software to JPL.

Data availability

All data used in this study are publicly available. Satellite altimetry AltiKa and SA6 and Jason-3 data from <https://podaac.jpl.nasa.gov/dataset/>. DART data from <https://www.ndbc.noaa.gov/obs.shtml?lat=13&lon=-173&zoom=2&pgm=tsunami>. Air-pressure and tide-gauge data from <http://www.bom.gov.au/pacific/>, <https://www.ioc-sealevelmonitoring.org/> and <https://www.met.gov.fj/>.

Received: 5 April 2024; Accepted: 12 September 2024;

Published online: 30 September 2024

References

- Donner, S. et al. The January 2022 Hunga Volcano explosive eruption from the multi technological perspective of CTBT monitoring. *Geophys. J. Int.* **235**, 48–73 (2023).
- NASA. Dramatic change at hunga tonga-hunga ha'apai. <https://earthobservatory.nasa.gov/images/149367/dramatic-changes-at-hunga-tonga-hunga-haapai> (2022).
- Duncombe, J. The surprising reach of Tonga's giant atmospheric waves. *Eos* **103** <https://doi.org/10.1029/2022EO220050> (2022).
- Lee, L. Tonga eruption made waves in Earth's ionosphere. *Eos* **103** <https://doi.org/10.1029/2022EO220202> (2022).
- Wright, C. J. et al. Surface-to-space atmospheric waves from Hunga Tonga-Hunga Ha'apai eruption. <https://doi.org/10.1038/s41586-022-05012-5> (2022).
- Kubota, T., Saito, T. & Nishid, K. Global fast-traveling tsunamis driven by atmospheric Lamb waves on the 2022 Tonga eruption. *Science* **377**, 91–94 (2022).
- Imamura, F. et al. Preliminary observations and impact in Japan of the Tsunami Caused by the Tonga volcanic eruption on January 15, 2022. *Pure Appl. Geophys.* **179**, 1549–1560 (2022).
- Tanioka, Y., Yamanaka, Y. & Nakagaki, T. Characteristics of the deep sea tsunami excited offshore Japan due to the air wave from the 2022 Tonga eruption. *Earth Planets Space* **74**, 1–7 (2022).
- Borrero, J. C. et al. Tsunami Runup and Inundation in Tonga from the January 2022 eruption of Hunga Volcano. *Pure Appl. Geophys.* **180**, 1–22 (2023).
- World Bank Assessment. <https://www.worldbank.org/en/news/press-release/2022/02/14/tonga-volcanic-eruption-and-tsunami-world-bank-disaster-assessment-report-estimates-damages-at-us-90m> (2022).
- Pelinovsky, E., Choi, B. H., Stromkov, A., Didenkulova, L. & Kim H.S. Analysis of tide-gauge records of the 1883 Krakatau tsunami. In: K. Satake (ed.), *Tsunamis: Case Studies and Recent Developments* **23**, 57–78 (2005).
- Bryant, E. *Tsunami: the underrated hazard*, Pp320 (Cambridge University Press, New York, 2001).
- Lamb, H. On the vibrations of an elastic sphere. *Proc Lond. Math. Soc.* **s1-13**, 189–212 (1881).
- Simkin, T. & Fiske, R. S. *Krakatau 1983: the volcanic eruption and its effects*. Washington, D.C.: Smithsonian Institution Press, Pp 646 (1983).
- BNPB. Tsunami Selat Sunda. BNPB–National Disaster Management Agency. <https://bnpb.go.id/berita/tsunami-selat-sunda> (2019).
- Ye, L. et al. The 22 December 2018 tsunami from flank collapse of Anak Krakatau volcano during eruption. *Sci. Adv.* **6**, eaaz1377 (2020).
- Schindele, F. et al. A review of tsunamis generated by volcanoes (TVG) source mechanism, modeling, monitoring and warning systems. *Pure Appl. Geophys.* <https://doi.org/10.1007/s00024-024-03515-y> (2024).
- Francis, P. W. The origin of the 1883 Krakatau tsunami. *J. Volcanol. Geotherm. Res.* **25**, 349–363 (1985).
- Paris R. Source mechanisms of volcanic tsunamis. *Phil. Trans. R. Soc.* **A 373**, <https://doi.org/10.1098/rsta.2014.0380> (2015).
- Nomanbhoy, N. & Satake, K. Generation mechanism of tsunamis from the 1883 Krakatau eruption. *Geophys. Res. Lett.* **22**, 509–512 (1995).
- Omira, R. et al. Global Tonga tsunami explained by a fast-moving atmospheric source. *Nature* **609**, 734–740 (2022).
- Ren, Z., Higuera, P. & Liu, P. L.-F. On tsunami waves induced by atmospheric pressure shock waves after the 2022 Hunga Tonga-Hunga Ha'apai volcano eruption. *J. Geophys. Res. Oceans* **128**, e2022JC019166 (2023).
- Pakoksung, K., Suppasri, A. & Imamura, F. The near-field tsunami generated by the 15 January 2022 eruption of the Hunga Tonga-Hunga Ha'apai volcano and its impact on Tongatapu, Tonga. *Sci. Rep.* <https://doi.org/10.1038/s41598-022-19486-w> (2022).
- Purkis, S. J. et al. The 2022 Hunga-Tonga megatsunami: near-field simulation of a once-in-a-century event. *Sci. Adv.* **9**, ead5493 (2023).
- Lynett, P. et al. Diverse tsunamigenesis triggered by the Hunga Tonga-Hunga Ha'apai eruption. *Nature*. <https://doi.org/10.1038/s41586-022-05170-6> (2022).
- Mackay, K. Digital elevation models of Hunga Volcano; pre- and post-15 January 2022 eruption. *Zenodo* <https://doi.org/10.5281/zenodo.7456324> (2022).
- Le Mével, H., Miller, C. A., Ribó, M., Cronin, S. & Kula, T. The magmatic system under Hunga volcano before and after the 15 January 2022 eruption. *Sci. Adv.* **9**, eadh3156 (2023).
- Doman, M. & Palmer A. The 'mind-blowing' sea floor changes caused by Tongan volcanic eruption, <https://www.abc.net.au/news/2022-11-21/sea-floor-map-reveals-huge-cavity-left-behind-by-tonga-volcano/101674708> (2022).
- Proudman, J. The effects on the sea of changes in atmospheric pressure. *Geophys. Supp. Mon. Not. R. Astronom. Soc.* **2**, 197–209 (1929).
- Liu, P. L.-F. & Higuera, P. Water waves generated by moving atmospheric pressure: theoretical analyses with applications to the 2022 Tonga event. *J. Fluid Mech.* **951**, A34 (2022).
- Park, H. & Cox, D. T. Empirical wave run-up formula for wave, storm surge and berm width. *Coast. Eng.* **115**, 67–78 (2016).
- Paprotny, D., Andrzejewski, P., Terefenko, P. & Furmanczyk, K. Application of empirical wave run-up formulas to the Polish Baltic Sea Coast. *PLoS One* **9**, e105437 (2014).
- Shokin, Y. I., Chubarov, L. B., Novikov, V. A., Sudakov A. N. Calculations of tsunami travel times in the Pacific Ocean (models, algorithms, techniques, results). *Sci. Tsunami Hazards*. **5**, (1987).
- Song, Y. T. & Haidvogel, D. A semi-implicit primitive equation ocean circulation model using a generalized topography-following coordinate system. *J. Comput. Phys.* **115**, 228–244 (1994).
- Shchepetkin, A. & McWilliams, J. C. The regional oceanic modelling system (ROMS): a split-explicit, free surface, topography-following-coordinate oceanic model. *Ocean Model.* **9**, 347–404 (2005).
- Satake, K. Linear and nonlinear computations of the 1992 Nicaragua earthquake tsunami. *PAGEOPH* **144**, 455–470 (1995).
- Song, Y. T. et al. The role of horizontal impulses of the faulting continental slope in generating the 26 December 2004 Tsunami. *Ocean Model.* <https://doi.org/10.1016/j.ocemod.2007.10.007> (2008).
- Song, Y. T., Fukumori, I., Shum, C. K. & Yi, Y. Merging tsunamis of the 2011 Tohoku-Oki earthquake detected over the open ocean. *Geophys. Res. Lett.* <https://doi.org/10.1029/2011GL050767> (2012).
- Amores, A. et al. Numerical simulation of atmospheric Lamb waves generated by the 2022 Hunga-Tonga volcanic eruption. *Geophys. Res. Lett.* **49** <https://doi.org/10.1029/2022GL098240> (2022).
- NOAA NDBC: <https://www.ndbc.noaa.gov/obs.shtml?lat=13&lon=-173&zoom=2&pgm=tsunami>.
- Song, Y. T. et al. The 26 december 2004 Tsunami source estimated from satellite radar altimetry and seismic waves. *Geophys. Res. Lett.* **23** <https://doi.org/10.1029/2005GL023683> (2005).
- Lytton, C., Hawkins, D., Abbott, M. Tan, S. & Hulley-jones, F. The day an underwater volcano almost wiped out a nation—*The Washington Post*. <https://apple.news/AKXWUyOOTCq-NQCTtFBNfQ> (2023).

43. Chen, K., Liu, Z. & Song, Y. T. Automated GNSS and teleseismic earthquake inversion (AutoQuake Inversion) for tsunami early warning: retrospective and real-time results. *PAAG* <https://doi.org/10.1007/s00024-019-02252-x> (2019).
44. Chen, K. et al. Triggering of the Mw 7.2 Hawaii earthquake of May 4, 2018 by a dike intrusion. *Geophys. Res. Lett.* <https://doi.org/10.1029/2018GL081428> (2019b).
45. Fu, L.-L. Pattern and velocity of propagation of the global ocean eddy variability. *J. Geophys. Res. Oceans* **114**, C11017 (2009).

Acknowledgements

The research described here was conducted at the Jet Propulsion Laboratory (JPL), California Institute of Technology, under contracts with the National Aeronautics and Space Administration (NASA). We thank Dr. Kejie Chen for providing the seismic inversion data, and Robert Greenwood of the Climate & Oceans Support Program in the Pacific (COSPPac), the Australian Bureau of Meteorology, for the tide-gauge data.

Author contributions

All authors contributed to this research. Y.T.S. and J.K.W. conceived this study. Y.T.S. analyzed air pressure and tide-gauge data. P.S.C., J.D.M.D., and S.F. performed satellite altimetry data. J.K.W. and Y.T.S. performed the analysis and interpretation of the results. All authors contributed to writing and editing the manuscript.

Competing interests

The authors declare no competing interests.

Additional information

Supplementary information The online version contains supplementary material available at <https://doi.org/10.1038/s43247-024-01694-z>.

Correspondence and requests for materials should be addressed to Y. Tony Song.

Peer review information *Communications Earth & Environment* thanks Andrea Verolino and the other, anonymous, reviewer(s) for their contribution to the peer review of this work. Primary Handling Editors: Domenico Doronzo and Carolina Ortiz Guerrero. A peer review file is available.

Reprints and permissions information is available at <http://www.nature.com/reprints>

Publisher's note Springer Nature remains neutral with regard to jurisdictional claims in published maps and institutional affiliations.

Open Access This article is licensed under a Creative Commons Attribution-NonCommercial-NoDerivatives 4.0 International License, which permits any non-commercial use, sharing, distribution and reproduction in any medium or format, as long as you give appropriate credit to the original author(s) and the source, provide a link to the Creative Commons licence, and indicate if you modified the licensed material. You do not have permission under this licence to share adapted material derived from this article or parts of it. The images or other third party material in this article are included in the article's Creative Commons licence, unless indicated otherwise in a credit line to the material. If material is not included in the article's Creative Commons licence and your intended use is not permitted by statutory regulation or exceeds the permitted use, you will need to obtain permission directly from the copyright holder. To view a copy of this licence, visit <http://creativecommons.org/licenses/by-nc-nd/4.0/>.

© The Author(s) 2024